Cluster states of multiple ferrimagnetic spheres in cavity magnonics

Anil Kumar Chauhan [*] and Jason Twamley [†]
Quantum Machines Unit, Okinawa Institute of Science and Technology Graduate University, Onna, Okinawa 904-0495, Japan

(Received 10 July 2025; accepted 15 December 2025; published 8 January 2026)

We present a scheme to generate the macroscopic Gaussian cluster states of multiple ferrimagnetic spheres in a microwave cavity through Kerr interactions. When each such sphere with self-Kerr nonlinearity is coupled to a single-cavity mode, it allows the generation of multimode entanglement and graph states—an important resource for one-way quantum computing through measurement-based protocols—near the strong and in the weak coupling regimes. While optimizing such states over the parameters governing the dynamics, the optimal appears for a far-detuned as well as dissipative cavity. Cluster states for a linear and a ring topology of a few spheres are discussed in the steady state of the system, further applicable to multiple spheres ($n = 10$), for experimentally feasible parameters.

DOI: 10.1103/6cpk-xcw4

I. INTRODUCTION

The deterministic generation of nonclassical states is an essential resource for quantum information [1,2], sensing and metrology [3], and to test the fundamentals of quantum mechanics [4]. Specifically, the Gaussian multipartite entanglement is crucial for large-scale quantum computing through measurement-based protocols [5–7]. This further requires non-Gaussian states [8,9] and their measurements for full implementation, though the Gaussian states remain central to quantum technologies. In such systems, the information is encoded in the quadrature eigenstates of modes, known as qumodes. Scaling entanglement to large qumodes is a key feature for quantum applications ranging from information processing [1], quantum network [10], and computing, and their further implementations by a sequence of measurements [11]. Among the multimode entangled states, cluster (graph) states [12–19] provide high scalability for quantum information processing and one-way quantum computing through measurement-based protocols [5,11,20,21]. The deterministic generation of such states is a potential framework for scaling and generating higher-dimensional states [22]. Therefore, the engineering of such states through nonlinear interactions in a suitable platform is a valuable resource for the upcoming quantum technologies.

The Gaussian cluster states have been studied in various platforms with different domains ranging from spatial [23,24], time [25–28], to frequency domain [29–32] and in their hybrid assemblies [33–35]. Generating such states in stationary spatial modes rather than propagating ones, such as the steady states of oscillators in optomechanics driven with multitone [36,37], is a promising candidate for information processing, storage, integrated quantum devices, and scalable quantum technologies. However, scaling to multiple oscillators within an optical cavity of such systems remains challenging in experiments [38]. Hybrid systems [39], being versatile in coupling to degrees of freedom and ranging from strong to ultrastrong couplings with low dissipation rates, provide a promising platform to explore such states.

Recently, hybrid systems of cavity magnonics [40–43] have attracted quite an interest in exploring macroscopic quantum phenomena through collective excitations of spins, in a yttrium iron garnet (YIG; $Y_3Fe_5O_{12}$) sphere within a microwave (MW) cavity, known as magnons. These modes can couple to varieties of additional degrees of freedom [44–47], making such hybrid systems a toolbox for upcoming quantum technologies [48,49], for example, magnetostrictive interaction through coupling to acoustic modes [45,50–53], coupling to superconducting qubit [44,54,55], three-body interaction of magnon-photon via center-of-mass motion [56,57], and coupling to higher-order magnetostatic modes [45], which further give rise to nonlinear interactions [58,59]. Specifically, the nonlinear interactions, such as magnetostrictive interaction, facilitate Gaussian squeezing of magnon and MW photons [60,61], which further enable entanglement [62] among them. The magnon squeezing has been explored in various platforms [63–65], in addition to a YIG in an MW cavity, making magnons a potential candidate for the engineering and realization of quantum devices. Very recently, cavity magnonics has been scaled up with multiple spheres of size 2 mm in a linear array within an MW cavity [66], making it a promising platform to explore multimode entanglement.

Specifically, the magnons have intrinsic magnetocrystalline anisotropy [67–69] induced by spin-orbit interaction that gives the magnon a Kerr nonlinearity. These nonlinear interactions are weak in strength but can be enhanced through input fields and used to generate nonclassical states. Using such versatile nonlinear interactions [70], systems can show bistability [71], multistability [72], nonlinear spin excitations [73], and squeezed states and entanglement [74] in the strong

[*]Contact author: anil.kumar@oist.jp
[†]Contact author: jason.twamley@oist.jp

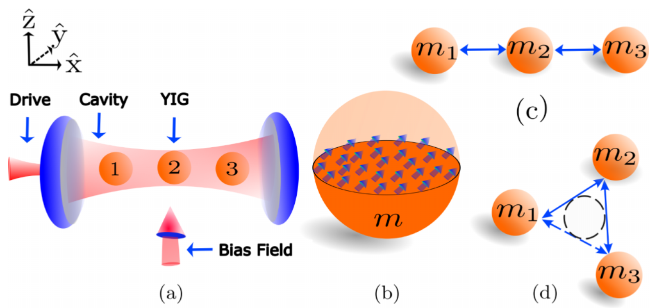

FIG. 1. (a) Schematic diagram of multiple ($n = 3$) YIG spheres (orange) in an MW cavity (reddish) with the polarization of the cavity along the y axis. A homogeneous bias field to the YIG spheres is orthogonal (along the z axis) to the optical axis. (b) Collective excitations of spins (magnons) in a YIG sphere. Topologies of graphs for three spheres: (c) a linear chain and (d) a ring structure for the generation of cluster states.

coupling regime. The versatility of nonlinear interactions is not limited to strong coupling only, and unlocking its potential through the optimization of nonclassical states [57], over the parameters governing the dynamics of the system, is required to extract the optimal states. This further facilitates scaling up entanglement from a few-body to a many-body system, though the optimization of parameters becomes necessary while dealing with multimode and nonlinear interactions.

Here, we consider an array of YIG spheres, each with intrinsic Kerr nonlinearity, inside an MW cavity collectively coupled to a single-cavity mode. The nonlinearities cause a frequency shift in each magnon mode, which further gets enhanced by multiple magnon modes. Driving the cavity on the negative detuning allows the creation of a two-mode squeezing interaction with the magnon and generates entanglement between cavity and magnon modes, and further among magnons. Specifically, multiple spheres shift cavity detuning far off the resonance, though they require large power and small magnon detunings to enhance the mean magnon through weak nonlinearities, and consequently require a large cavity-decay rate to cool the system. Note that the deterministic generation of nonclassical steady states of the system is of particular interest in integrated devices and for upcoming quantum technologies, rather than the radiative one, as the generated state remains forever as long as the drive is on. Using this framework, we present the generation of stationary multimode entanglement and cluster states for the different topologies of a few YIG spheres near the strong and in the weak cavity-magnon coupling regimes. However, the optimization of cluster state over parameters prefers an MW cavity to the latter and is favorable in the dissipative regime. Further, generalizing this proposal to multiple spheres allows us to entangle $n = 10$ YIG spheres with a single-cavity mode and without the requirement of driving with multitone frequencies and multiple cavity modes.

II. MULTIPLE YIG SPHERES

We consider an array of n YIG spheres inside an MW cavity, as shown in Fig. 1, with Kerr nonlinearity in each of them while placed at a distance $d > 2r$ [66], where r is the radius of the sphere, to avoid direct coupling between them. Magnons are the collective excitations of spins ($n_s \approx 10^{19}$) [54], as shown in Fig. 1(b).

The Hamiltonian for such a system can be written as

$$H = \omega_a a^\dagger a + \sum_{j=1}^{n} \omega_{m_j} m_j^\dagger m_j + \sum_{j=1}^{n} g_j (a^\dagger m_j + a m_j^\dagger) + \sum_{j=1}^{n} K_j (m_j^\dagger m_j m_j^\dagger m_j) + E_d (a e^{i\omega_l t} + a^\dagger e^{-i\omega_l t}), \quad (1)$$

where operators a and m_j correspond to MW cavity and jth magnon modes, and ω_l is the frequency of MW drive field $E_d = \sqrt{\kappa_a P_{mw}/\hbar\omega_l}$, polarized along orthogonal to the bias field's direction, with associated linewidth of cavity mode κ_a and power P_{mw}. The interaction strength between a cavity mode and a magnon mode m_j is denoted by g_j. The size of the YIG sphere, MW cavity mode volume, and location inside the MW cavity allow us to tune the cavity-magnon couplings [40] from a weak $g_j < \kappa_a, \gamma_{m_j} \ll \omega_{m_j}$, to a strong $0.1\omega_{m_j} > g_j > \kappa_a, \gamma_{m_j}$, and to an ultrastrong $\omega_{m_j} > g_j > 0.1\omega_{m_j} \gg \kappa_a, \gamma_{m_j}$ regime [75–77], where γ_{m_j} is the linewidth of the magnon mode m_j. The term K_j represents the self-Kerr effect (see Sec. S1 of the Supplemental Material [78]) of each magnon mode induced due to spin-orbit interactions causing magnetocrystalline anisotropy [68]. Note that the frequency of the uniform magnon mode (Kittel mode) depends linearly on the bias field, $\omega_m = \gamma|\vec{B}_0| + \omega_{m,0}$ [40,71], where $\gamma = 28$ GHz/T is the gyromagnetic ratio, $\vec{B}_0$ is the biased field amplitude, and $\omega_{m,0}$ is given by the anisotropy field. The YIG sphere possesses total number of spins $n_s s = \rho V_0$, for volume V_0 of the sphere with $\rho = 4.22 \times 10^{27}$ m^{-3} the spin density while driven with MW field and $s = 5/2$ denotes the spin number of the ground-state Fe^{3+} ion in YIG [40].

In the rotating frame of the driving MW field with frequency ω_l, the system Hamiltonian becomes

$$H = \Delta\omega_a a^\dagger a + \sum_{j=1}^{n} \Delta\omega_{m_j} m_j^\dagger m_j + \sum_{j=1}^{n} g_j (a^\dagger m_j + a m_j^\dagger) + \sum_{j=1}^{n} K_j (m_j^\dagger m_j m_j^\dagger m_j) + E_d (a + a^\dagger), \quad (2)$$

where $\Delta\omega_{a,m_j} = \omega_{a,m_j} - \omega_l$. The equations of motion for such a system can be written as

$$\dot{a} = -i\left(\Delta\omega_a - i\frac{\kappa_a}{2}\right)a - i\sum_{j=1}^{n} g_j m_j - iE_d + \sqrt{\kappa_a} a_{in},$$
$$\dot{m}_j = -i\left(\Delta\omega_{m_j} - i\frac{\gamma_{m_j}}{2}\right)m_j - ig_j a - 2iK_j m_j m_j^\dagger m_j + \sqrt{\gamma_{m_j}} m_{j,in}, \quad (3)$$

where the input noise for cavity a_{in} and magnon $m_{j,in}$ modes follows the correlations $\langle O_{in}(t) O_{in}^\dagger(t')\rangle = (n_{th}^O(\omega) + 1)\delta(t - t')$ and $\langle O_{in}^\dagger(t) O_{in}(t')\rangle = (n_{th}^O(\omega))\delta(t - t')$, where $n_{th}^O(\omega) = [\exp(\hbar\omega_O/k_B T) - 1]^{-1}$ ($O = m_j, a$ with associated frequency of each mode ω_O) is the mean thermal occupation of each mode at temperature T, respectively.

While the cavity mode is strongly driven, the amplitudes of mean photons $\langle a\rangle \gg 1$ and magnons $\langle m_j\rangle \gg 1$ (due to the strong cavity-magnon beam splitter coupling) are very large at the steady state. This allows us to use the standard linearization technique, $O = \langle O\rangle + \delta O$, where $\langle O\rangle$ is the mean and δO is the fluctuation around the mean value of any operator O. The steady-state solution $\langle \dot{O}\rangle = 0$ ($O = a, m_j$) of the mean equations in Eq. (3) is given by

$$\langle \alpha\rangle = -\frac{E_d}{\sum_{j=1}^{n}\frac{g_j^2}{\left(\tilde{\Delta}\omega_{m_j} - i\frac{\gamma_{m_j}}{2}\right)} - \left(\Delta\omega_a - i\frac{\kappa_a}{2}\right)}, \tag{4}$$

$$\langle M_j\rangle = \frac{-E_d g_j}{\left[\sum_{k=1}^{n}\frac{g_k^2}{\left(\tilde{\Delta}\omega_{m_k} - i\frac{\gamma_{m_k}}{2}\right)} - \left(\Delta\omega_a - i\frac{\kappa_a}{2}\right)\right]\left(\tilde{\Delta}\omega_{m_j} - i\frac{\gamma_{m_j}}{2}\right)}, \tag{5}$$

where $\langle\alpha\rangle$ and $\langle M_j\rangle$ are the means of modes a and m_j, respectively. The shift in the magnon detunings is denoted by $\tilde{\Delta}\omega_{m_j} = \Delta\omega_{m_j} + 4K_J|\langle M_j\rangle|^2$, $j, k = \{1, 2, 3, \ldots, n\}$.

Therefore, the fluctuation equations of motion can be written as

$$\begin{aligned}\dot{\delta a} &= -i(\Delta\omega_a - i\kappa_a/2)\delta a - i g_j\delta m_j + \sqrt{\kappa_a}\delta a_{in},\\ \dot{\delta m_j} &= -i(\tilde{\Delta}\omega_{m_j} - i\gamma_{m_j}/2)\delta m_j - i(g_j\delta a + \tilde{K}_j\delta m_j^{\dagger})\\ &\quad + \sqrt{\gamma_{m_j}}\delta m_{j,in},\end{aligned} \tag{6}$$

where $\tilde{K}_j = 2K_j\langle M_j\rangle^2$.

III. STEADY-STATE SOLUTION FOR A FEW SPHERES, $n = 3$

We choose a simple case of $n = 3$ spheres inside an MW cavity, as shown in Fig. 1. For three YIG spheres, we have two topologies of the graph states, i.e., a linear chain as in Fig. 1(c) and a ring structure as in Fig. 1(d), thanks to the coupling of multiple spheres through a common cavity mode. To find the steady state of the system, we start from the Langevin equations in matrix form

$$\dot{r} = Ar + \xi, \tag{7a}$$

$$r = (X_1, P_1, X_2, P_2, X_3, P_3, X_4, P_4)^T, \tag{7b}$$

$$\xi = (\sqrt{\gamma_{m_1}}X_{1,\mathrm{in}}, \sqrt{\gamma_{m_1}}P_{1,\mathrm{in}}, \sqrt{\gamma_{m_2}}X_{2,\mathrm{in}}, \sqrt{\gamma_{m_2}}P_{2,\mathrm{in}}, \sqrt{\gamma_{m_3}}X_{3,\mathrm{in}}, \sqrt{\gamma_{m_3}}P_{3,\mathrm{in}}, \sqrt{\kappa_a}X_{4,\mathrm{in}}, \sqrt{\kappa_a}P_{4,\mathrm{in}})^T, \tag{7c}$$

$$A = \begin{pmatrix} \gamma_{m_{1+}} & \Delta\omega_{m_{1+}} & 0 & 0 & 0 & 0 & 0 & g_1\\ \Delta\omega_{m_{1-}} & \gamma_{m_{1-}} & 0 & 0 & 0 & 0 & -g_1 & 0\\ 0 & 0 & \gamma_{m_{2+}} & \Delta\omega_{m_{2+}} & 0 & 0 & 0 & g_2\\ 0 & 0 & \Delta\omega_{m_{2-}} & \gamma_{m_{2-}} & 0 & 0 & -g_2 & 0\\ 0 & 0 & 0 & 0 & \gamma_{m_{3+}} & \Delta\omega_{m_{3+}} & 0 & g_3\\ 0 & 0 & 0 & 0 & \Delta\omega_{m_{3-}} & \gamma_{m_{3-}} & -g_3 & 0\\ 0 & g_1 & 0 & g_2 & 0 & g_3 & -\frac{\kappa_a}{2} & \Delta\omega_a\\ -g_1 & 0 & -g_2 & 0 & -g_3 & 0 & -\Delta\omega_a & -\frac{\kappa_a}{2} \end{pmatrix}, \tag{7d}$$

where $\gamma_{m_{j\pm}} = -\frac{\gamma_{m_j}}{2} \pm \mathrm{Im}(\tilde{K}_j)$ and $\Delta\omega_{m_{j\pm}} = \pm\tilde{\Delta}\omega_{m_j} - \mathrm{Re}(\tilde{K}_j)$ for j = 1, 2, 3. We use the quadrature operators for the magnon $X_k = (\delta X_k + \delta X_k^{\dagger})/\sqrt{2}$, $P_k = -i(\delta P_k - \delta P_k^{\dagger})/\sqrt{2}$, $k = 1, 2, 3$ for δm_j, and $k = 4$ for the cavity mode δa. The steady state of the system can now be expressed in terms of the covariance matrix, which obeys the Lyapunov equation

$$AV + VA^T + D = 0, \tag{8}$$

where V with elements $V_{jl} = \langle r_j r_l + r_l r_j\rangle - 2\langle r_j\rangle\langle r_l\rangle$ is the covariance matrix of the system's Wigner function and

$$\begin{aligned} D &= \langle \xi(t)\xi^T(t)\rangle\\ &= \mathrm{diag}\big[\gamma_{m_1}(2n_{th}^{m_1}+1), \gamma_{m_1}(2n_{th}^{m_1}+1), \gamma_{m_2}(2n_{th}^{m_2}+1),\\ &\quad \gamma_{m_2}(2n_{th}^{m_2}+1), \gamma_{m_3}(2n_{th}^{m_3}+1), \gamma_{m_3}(2n_{th}^{m_3}+1),\\ &\quad \kappa_a(2n_{th}^{a}+1), \kappa_a(2n_{th}^{a}+1)\big] \end{aligned} \tag{9}$$

is the diffusion matrix. To ensure the stability of the system, we only consider the steady solution for which all the eigenvalues of a drift matrix have negative real part [79].

IV. CLUSTER STATES

Cluster (graph) states are multimode entanglement, which are fundamental resources for measurement-based one-way quantum computing, quantum metrology, and quantum networks. These states are nearly zero-momentum eigenstates [6] that allow the building of a quantum network and selectively transporting quantum states. In general, cluster states are orthogonal (such as Einstein-Podolsky-Rosen (EPR) states) and get destroyed when measured, making it one-way. In the limit of infinite squeezing, the n-mode cluster states satisfy certain quadrature correlations [6,15,80], known as nullifiers (see Sec. S2 of the Supplemental Material [78]), which follow

$$\left\langle \Delta\left(P_j - \sum_{k\in G_j} X_k\right)^2\right\rangle \to 0, \quad \forall\ j \in G, \tag{10}$$

where the indices $j \in G$ represent the vertices of the graph G, $k \in G_j$ are the nearest neighbors of the mode j, and $\Delta(O) = \langle O^2\rangle - \langle O\rangle^2$ is the variance of the operator O. In such a case, the graph state becomes a simultaneous zero eigenstate of those quadratures' n linear combinations. Note that the infinite squeezing requires infinite energy and cannot be normalized; thus, it is unphysical. However, the approximated cluster states, with finite squeezing, follow a sufficient condition given by inequalities [15–19,21] as

$$\left\langle \Delta\left(P_j - \sum_{k\in G_j} X_k\right)^2\right\rangle < 2, \quad \forall\ j \in G, \tag{11}$$

which can further be written as

$$\left\langle \Delta\left(P_j - X_k - \sum_{t\in G_{j|k}} X_t\right)^2\right\rangle + \left\langle \Delta\left(P_k - X_j - \sum_{l\in G_{k|j}} X_l\right)^2\right\rangle < 4, \tag{12}$$

where $t \in G_{j|k}$ denotes the set of all neighbor modes of the jth mode except for the kth mode. This equation means that the jth and kth modes are entangled. For the three modes, we consider two relevant topologies, i.e., a linear chain as in Fig. 1(c), and a ring as in Fig. 1(d).

Using the above inequalities, we have a set of nullifiers for a chain of three modes [17,18],

$$\begin{aligned} N_1^c &= \langle \Delta(P_1 - X_2)^2\rangle > N_{1,0}^{(c)},\\ N_2^c &= \langle \Delta(P_2 - X_1 - X_3)^2\rangle > N_{2,0}^{(c)},\\ N_3^c &= \langle \Delta(P_3 - X_2)^2\rangle > N_{3,0}^{(c)}, \end{aligned} \tag{13}$$

where nullifiers N_j^c denote the modes in a linear chain fashion, as shown in Fig. 1(c) and vacuum noise in each is denoted by $N_{j,0}^{(c)}$. Violating the above inequalities allows the generation of a cluster state in a linear chain topology. These inequalities are determined by excess vacuum noise due to the nearest neighbor in the respective momentum quadratures, similar to the optical modes [15].

Further, the generation of cluster state and multimode entanglement [81] for different topologies can be verified using the violation of the following inequalities [23]:

$$\begin{aligned} N_1^c + N_2^c &> N_{1,0}^{(c)} + N_{2,0}^{(c)},\\ N_2^c + N_3^c &> N_{2,0}^{(c)} + N_{3,0}^{(c)}, \end{aligned} \tag{14}$$

which stems from Eq. (13). Using the cyclic permutations of the three modes (momentum quadratures), we can consider the other set of possible combinations. However, we focus here on only one set of nullifiers, and the interplay among the rest of the combinations can be understood from the common combinations of quadratures in chain and ring topologies. For example, the nullifier N_2^c in the linear chain is equal to N_2^r in the ring topology (as shown below). Similarly, for a ring topology of three modes, as shown in Fig. 1(d), we consider the following inequalities:

$$\begin{aligned} N_1^r &= \langle \Delta(P_1 - X_2 - X_3)^2\rangle > N_{1,0}^{(r)},\\ N_2^r &= \langle \Delta(P_2 - X_3 - X_1)^2\rangle > N_{2,0}^{(r)},\\ N_3^r &= \langle \Delta(P_3 - X_1 - X_2)^2\rangle > N_{3,0}^{(r)}. \end{aligned} \tag{15}$$

Since the modes are coupled to each other (nearest neighbor), the nullifiers violating the above inequities, going below the shot noise, will suffice for the generation of cluster states. Note that the nullifiers are orthogonal to each other and follow $[N_1^{c,r}, N_2^{c,r}] = [N_2^{c,r}, N_3^{c,r}] = [N_1^{c,r}, N_3^{c,r}] = 0$. In addition, the gain in squeezing in dB can be calculated as $-10\log10(N_j^{(c,r)}/N_{j,0}^{(c,r)})$, where $N_{j,0}^{(c,r)}$ is the vacuum noise for the respective nullifier.

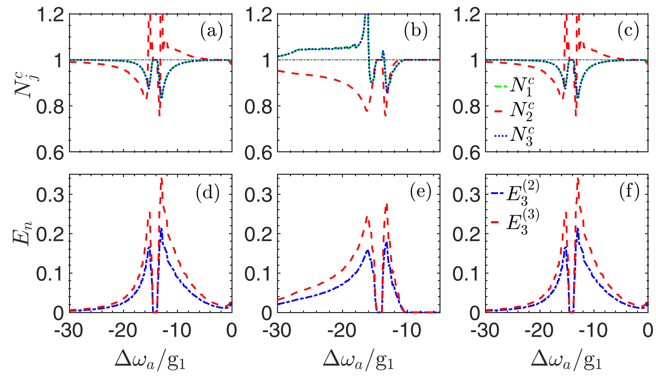

FIG. 2. Cluster state generation for a linear topology. Numerical optimization of nullifier, (a) N_1^c (dot-dashed green), (b) N_2^c (dashed red), and (c) N_3^c (dotted blue), over the drive power E_d, vs detuning $\Delta\omega_a/g_1$ for the minimum of each. We show the corresponding nullifiers in each case for the same optimal parameters. The vacuum noise level $N_{j,0}^c$ is shown by a dot-dashed line (black) in each top plot. Panels (d)–(f) show the corresponding entanglement in all pairs $E_3^{(2)}$ and all bipartitions $E_3^{(3)}$ for each top plot. The other parameters are $g_j/2\pi = \kappa_a/2\pi = 200$ MHz, $\tilde{\Delta}\omega_{m_j}/g_1 \approx -0.21$, $K_j/2\pi = -10$ nHz, $\gamma_{m_j}/2\pi = 1$ MHz, and $T = 100$ mK.

In Gaussian systems, squeezing is a necessary and sufficient condition to generate an entangled state of the system. The logarithmic negativity fully quantifies Gaussian entanglement [82]; however, the measurement of a pair of commuting operators is easier to verify experimentally, as in EPR variance of two modes. Therefore, the EPR variance [83,84] quantifies the entanglement between the modes through the simultaneous measurement of the variance of the summation of position $(X_1 + X_2)/\sqrt{2}$ and the difference of momentum quadratures $(P_1 - P_2)/\sqrt{2}$ below the vacuum noise. For higher modes, one can explore the squeezing among such joint combinations of X_j and P_j, where $j = 1, 2, 3, \ldots, n$, but we are interested in the inequalities given in Eqs. (13) and (15). The squeezing in those collective magnon modes is further verified by entanglement through the logarithmic negativity. For three modes, we study pairwise entanglement ($p = 2$) when entanglement in a pair of modes is obtained after tracing out the third mode, where each bipartition is formed by one mode only. Another type of entanglement includes the whole three-mode system ($p = 3$), where one bipartition is formed by one mode and the other bipartition by the remaining two modes. After quantifying the Gaussian entanglement through logarithmic negativity [82] for each bipartition, we use the following figures of merit [57,85] for the multimode entanglement:

$$E_3^{(p)} = \sqrt[3]{E_1E_2E_3}, \tag{16}$$

where $p = 2$ for two-mode and $p = 3$ for three-mode bipartitions of three magnon modes, and E_i denotes the logarithmic negativity of each bipartition. Any asymmetries in the system parameters will give rise to entanglement in a few bipartitions (see Sec. S5 of the Supplemental Material [78]).

V. RESULTS

We show the plots of cluster state generation in Fig. 2 for each nullifier of the linear chain topology, $N_{1,2,3}^c$, optimized over the drive power in the range $E_d = 0$–10^{10} MHz for minimum in each and plotted against the detuning $\Delta\omega_a/\mathrm{g}_1$. We begin the analysis with a symmetric case with equal cavity-magnon coupling $g_j \approx \kappa_a$ (near the strong coupling) as it can go ultrastrong (GHz) [40] and weak Kerr nonlinearity $K_j/2\pi = -10$ nHz [69]. We plot the optimal N_1^c (dot-dashed green) in panel (a), and corresponding N_2^c (dashed red) and N_3^c (dotted blue) at the same couplings and drive power to see the interplay among them. The remaining chosen parameters are $\mathrm{g}_j/2\pi = \kappa_a/2\pi = 200$ MHz, $\tilde{\Delta}\omega_{m_j}/\mathrm{g}_1 \approx -0.21$, $K_j/2\pi = -10$ nHz, $\gamma_{m_j}/2\pi = 1$ MHz, and $T = 100$ mK for $\omega_{a,m_j}/2\pi = 10$ GHz. The shot noise level $N_{j,0}^c$ is shown by the dot-dashed black line in panels (a)–(c).

Since $N_{1,3}^c$ consists of two magnon modes, the minimum of them remains slightly higher than N_2^c with three modes, as shown in Fig. 2(a). In the former, the third particle remains noisy and weakens the correlations rather than cooling all of them in N_2^c, which goes below $N_{1,3}^c$. This is further shown by optimizing N_2^c over power in panel (b). An additional sphere and Kerr nonlinearity will induce an extra shift in detunings for optimal nullifiers as in panel (b) for N_2^c. However, the corresponding nullifiers $N_{1,3}^c$ at the optimum of N_2^c go up compared to the previous plots. Note that reducing noise in some combinations of quadratures (in $N_{1,3}^c$) will be balanced by enhancing their canonical conjugate (in N_2^c). Furthermore, the nullifier $N_{1,3}^c$ with two modes goes to a minimum for the same detuning as both have the symmetric structure of two modes with two Kerr nonlinear terms. Therefore, optimizing N_3^c over powers, in panel (c), reveals similar behaviors as earlier in panel (a) due to symmetry in the system.

The strong correlation and optimal cluster state are further verified by the logarithmic negativity, where we plot multimode entanglement in all pairs $E_3^{(2)}$ (dot-dashed blue) and all bipartitions $E_3^{(3)}$ (dashed red) [57,85] in panels (d) and (e) corresponding to each top plot. The maximum in each corresponds to the minimum in each nullifier. However, while optimizing N_2^c, a slightly smaller value of entanglement is reached than in the other two cases, as here $N_{1,3}^c$ goes up and weakens the correlations. Thus, all pairs and all bipartitions can go simultaneously high in a common parameter regime, which is different from the former going completely zero [57] while the latter enhances. Note that the Kerr nonlinearity allows a versatile parameter regime (see Sec. S5 of the Supplemental Material [78]) with stable solutions on the positive axis of cavity and magnon detunings, and for positive Kerr nonlinearity as well. The gain-loss ($\pm$) energy balance can be seen from Eq. (7), where each quadrature energy $\gamma_{m_{j\pm}}$ depends upon K_j and similarly the transitions or cross- coupling between quadratures through $\Delta\omega_{m_{j\pm}}$. This clearly shows a broad range of parameter space for such systems. As long as the system is symmetric with equal magnon detunings, cavity-magnon couplings, self-Kerr terms, and dissipation rates, this will generate simultaneous entanglement in all the pairs $E_3^{(2)}$ and bipartitions $E_3^{(3)}$. Introducing any asymmetry will generate entanglement in some pairs and bipartitions rather than simultaneous entanglement in all of them (see Sec. S5 of the Supplemental Material [78]).

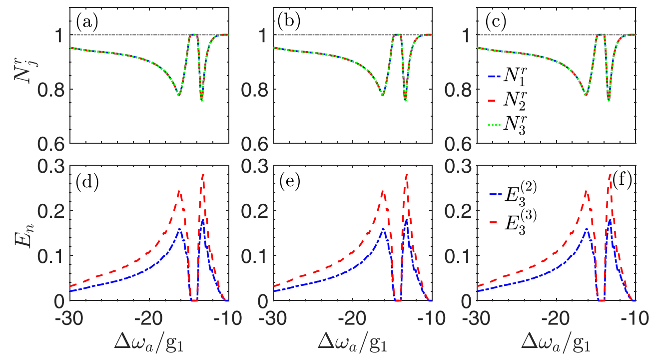

FIG. 3. Cluster state generation for a ring topology. Numerical optimization of nullifier, (a) N_1^r (dot-dashed blue), (b) N_2^r (dashed red), and (c) N_3^r (dotted green), over the drive power, vs detunings $\Delta\omega_a/\mathrm{g}_1$ for the minimum of each, along with corresponding nullifiers in each case for the same optimal parameters. The vacuum noise level $N_{j,0}^r$ is shown by a dot-dashed line (black) in each top plot. Panels (d)–(f) show the corresponding entanglement in all pairs $E_3^{(2)}$ and all bipartitions $E_3^{(3)}$ for each top plot. The other parameters remain the same as in Fig. 2.

Similarly, for the ring topology of the cluster state, we show the plots in Fig. 3 for the inequalities in Eq. (15), while optimizing over the power. We plot the optimal nullifier (a) for N_1^r (dot-dashed blue), (b) for N_2^r (dashed red), and (c) for N_3^r (dotted green), along with corresponding nullifiers for the same parameters in each case. When optimal N_1^r drops below the shot noise in panel (a), it simultaneously brings the other nullifiers $N_{2,3}^r$ below the shot noise and follows the same behavior in panels (b) and (c). The overlapping lines are obvious from the symmetry in the system with the same cavity-magnon couplings and equal Kerr nonlinearities for a symmetric structure in Eq. (15). Thus, breaking this symmetry as mentioned before, with unequal couplings, damping, and nonlinearities, will show a separate set of parameters to reach the optimal nullifier (see Sec. S5 of the Supplemental Material [78]). However, we focus here on the symmetric case only. The generation of cluster state is further supported by the corresponding entanglement in all pairs $E_3^{(2)}$ and all bipartitions $E_3^{(3)}$ as shown in panels (d)–(f) for the same parameters as in each optimal N_j^r. Interestingly, the ring topology forms a complete graph (all modes are connected to each other) and paves the way toward quantum network [86,87].

Since a single-cavity mode is coupled to multiple spheres, the cavity-magnon coupling near the strong-coupling regime leads to mode hybridization, which enhances the correlations but suppresses the cooling of the modes. However, cooling such collective modes should be efficient in the weak coupling regime. While the amplification due to magnon detunings and Kerr nonlinearity enhances the number of mean magnons and photons, the cavity decay will try to balance the dynamics through coupling to the reservoir rather than to the magnon, as in strong/ultrastrong cases. To further verify our intuition, we optimize each nullifier for its minimum over power and plot against the cavity detuning and linewidth in Figs. 4(a)–4(c). We plot the minimum in each case for a fixed linewidth κ_a/g_1 (g_1 is the same as in the previous plots in Figs. 2 and 3) across

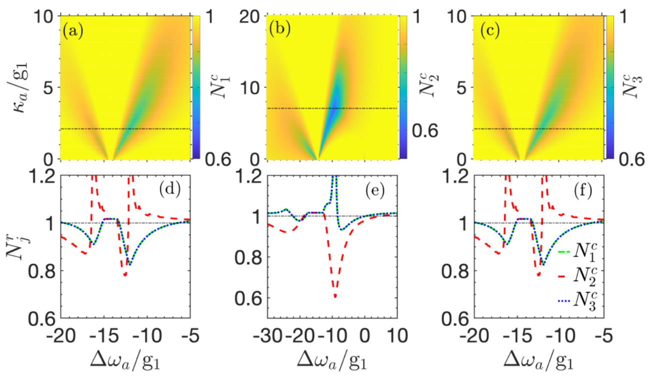

FIG. 4. Variation of nullifier against cavity detuning and linewidth normalized with cavity-magnon coupling g_1. Plots for optimal nullifiers, (a) N_1^c, (b) N_2^c, and (c) N_3^c, optimized over drive power. The line plots (d)–(f) correspond to a minimum of the nullifier along the line (dot-dashed black) for fixed κ_a/g_1 in each of the top plots. (d) For optimal N_1^c (dot-dashed green) along with corresponding N_2^c (dashed red) and N_3 (dotted blue). Similarly (e) for N_2^c and (f) for N_3^c. The rest of the parameters are the same as in Fig. 2.

the dotted-dashed black line in panels (a)–(c), against cavity detuning in panels (d)–(f) along with the other nullifiers at the same parameters. The nearly overlapped nullifiers in Fig. 2 now get separated as $N_{1,3}^c$ goes to minimum ($\approx$1 dB squeezing) around $\Delta\omega_a/g_1 \approx -12$ in panel (a) and N_2^c ($\approx$2.2 dB squeezing) around $\Delta\omega_a/g_1 \approx -10$ in panel (b). It is interesting to note that for optimal $N_{1,3}^c$ with two modes, the required linewidth turns out to be $\kappa_a/g_1 \approx 2$, which for N_2^c with three modes gives $\kappa_a/g_1 \approx 7$. These parameters show that the large number of modes requires less cavity detuning (more photons) than the few modes to get stronger correlations, and is further balanced by a large cavity-decay rate to cool the system.

For the ring topology of three modes, we plot the optimal nullifiers in Figs. 5(a)–5(c) for cavity detuning $\Delta\omega_a/g_1$ and decay rate κ_a/g_1. The cavity-decay rate corresponding to

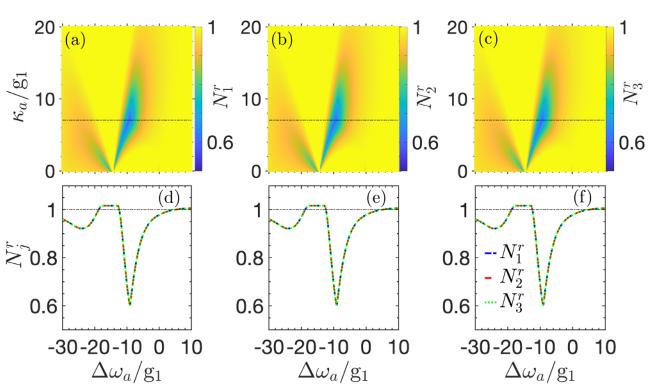

FIG. 5. Variation of nullifier against cavity detuning and linewidth normalized with cavity-magnon coupling g_1. Plots for optimal nullifiers, (a) N_1^r, (b) N_2^r, and (c) N_3^r, optimized over drive power. The line plots (d)–(f) correspond to a minimum of the nullifier along the line (dot-dashed black) for fixed κ_a/g_1 in each of the top plots. (d) For optimal N_1^r (dot-dashed blue) along with corresponding N_2^r (dashed red) and N_3 (dotted green). Similarly (e) for N_2^r and (f) for N_3^r. The rest of the parameters are the same as in Fig. 2.

the minimum in each case is denoted by a dot-dashed black horizontal line. The symmetric structure of the three modes for equal coupling to the cavity mode, equal dissipation, and Kerr nonlinearity brings all the three nullifiers to a minimum value simultaneously ($\approx$2.2 dB squeezing) as shown in plots (d)–(f) for a fixed value of $\kappa_a/g_1 \approx 7$ in each top plot. This symmetry makes the ring topology more favorable for generating the cluster state where all nullifiers reach a minimum simultaneously for the same set of parameters. This further generates entanglement in all bipartitions as shown in Fig. 3.

A. Cluster states for $n = 5$ and $n = 10$

Based on a nullifier of three modes in a linear or ring topology $N_2^{c,r}$, this scheme can be generalized to a large number of spheres in both a linear or two-dimensional (2D) array (see Fig. S2 of the Supplemental Material [78]). Similar to a common nullifier $N_2^{c,r}$ in three modes, this combination remains the same in higher multiple spheres, in linear and ring topologies. Therefore, this three-mode entanglement can serve as a unit cell to scale entanglement to higher modes or dimensions. In addition, the positive partial transpose criterion is a necessary and sufficient condition for separability of any bipartition of two and three modes, in the Gaussian regime [88]. As mentioned above, the nullifiers of the two modes and the three modes overlap in each case, respectively, due to symmetry in the systems. A slight shift in the parameters is expected, as caused by considering more modes in the topologies, though the nullifiers remain coincident in each case. Note that for the ring topologies, the number of rings with three modes for any n spheres is given by the combination ${}^nC_3 = n!/3!(n-3)!$. Here, we focus on the simple graphs of two and three modes without self-loops and multiple edges. Therefore, optimizing only one of them, again a common nullifier in chain topology, over parameters, will be enough to generate a cluster state of possible ring topologies, thanks to the symmetry in the system. For $n = 4$, we have a linear chain of four modes and many possible ring topologies of three modes (see Fig. S4 in Sec. S4 of the Supplemental Material [78]), and we expect the same behavior as in Fig. 5, except a slight shift in the plots due to the additional particle.

We show the plots in Fig. 6 for $n = 5$ and $n = 10$ modes. We optimize nullifiers over power ($E_d = 0$–10^{11} MHz) and cavity-decay rates and keep them fixed for $n = 5$ and $n = 10$ modes. Due to symmetry in the systems, We optimize one of the two- and three-mode nullifiers and plot the remaining ones for the same parameters. We optimize $N_{1,2}^c$ for $n = 5$ and $N_{9,10}^c$ for $n = 10$, though the first five nullifiers in the latter remain the same as in the former. For a linear chain of five (ten), the end nullifiers are of the two modes $N_j^c = \langle\Delta(P_j - X_{j+1/j-1})^2\rangle$, $j = 1, 5$ ($j = 1, 10$), and in between are of the three modes $N_j^c = \langle\Delta(P_j - X_{j+1} - X_{j-1})^2\rangle$, for $j = 2, 3, 4$ ($j = 2, 3, \ldots, 8, 9$). In Fig. 6(a), we plot the optimal N_1^c (solid red) versus $\Delta\omega_a/g_1$ for $\tilde{\Delta}\omega_{m_j}/g_1 \approx -0.23$, $\kappa_a/g_1 = 1.85$, $E_d = 7 \times 10^9$ MHz, and $g_j/2\pi = 550$ MHz. The inset shows the generated entanglement in all bipartitions $E_3^{(3)}$ of three-mode N_j^c for $j = 2, 3, 4$. Note that the entanglement in all bipartitions $E_3^{(3)}$ is generated along with all pairs $E_3^{(2)}$, as shown in Figs. 2 and 3, as long as the system is symmetric

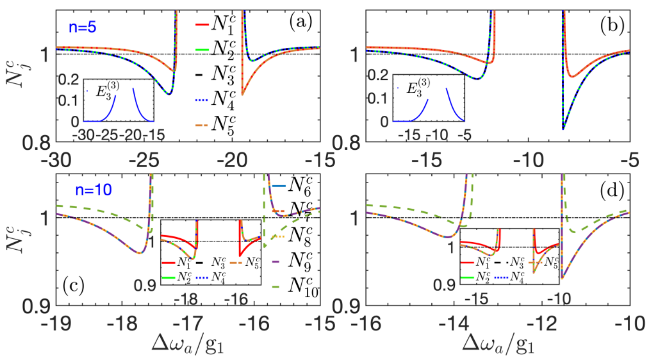

FIG. 6. Cluster state of multiple YIG spheres. We plot the nullifiers for a linear chain topology of $n = 5$; N_1^c (solid red) in panel (a) and N_2^c (solid green) in panel (b) for optimal κ_a and drive power, along with the other nullifiers N_3^c (dashed black), N_4^c (dotted blue), and N_5^c (dot-dashed brown) at the same optimal parameters. The inset shows entanglement in all bipartitions $E_3^{(3)}$ of three-mode nullifiers $N_{2,3,4}^c$. For $n = 10$, we plot the optimal N_{10}^c (dark green dashed) in panel (c) and N_9^c (purple dashed) in panel (d) along with the other nullifiers N_6^c (solid teal blue), N_7^c (dot-dashed brown), and N_8^c (dotted light brown) for the same parameters. The inset shows the first five combinations of nullifiers for $n = 10$.

with equal couplings, dissipations, and Kerr nonlinearities. The rest of the parameters are the same as in Fig. 2. The corresponding nullifiers N_2^c (solid green), N_3^c(dashed black), N_4^c (dotted black), and N_5^c (dot-dashed brown) are plotted for the same parameters.

We plot the three-mode nullifier, common in a ring and a linear topology, in Fig. 6(b) for optimal of N_2^c for $\tilde{\Delta}\omega_{m_j}/g_1 = -0.5$, $\kappa_a/g_1 = 2.5$, and $E_d = 3.2 \times 10^{10}$ MHz along with the corresponding nullifiers for the same parameters. The rest of the parameters are the same as in panel (a). The shift in the parameters is clearly seen for the optimal of the two- and three-mode nullifiers in panels (a) and (b), which makes optimization necessary. In addition, N_2^c drops much below in panel (b) than in panel (a). However, the corresponding two-mode nullifier $N_{1,5}^c$ goes up for this case and reduces entanglement slightly, as shown in the inset. In addition, for the ring topology, the nullifiers $N_{2,3,4}^c$ remain the same and drop simultaneously below the shot noise that generates entanglement among all such overlapping bipartitions and among five modes as well.

We further increase the number of YIG spheres ($n = 10$) in the same configurations and optimize $N_{9,10}^c$ as the first five nullifiers remain the same as in the previous case. The optimization becomes complex with a larger number of modes as the dimension of the system goes up. Therefore, we optimize a few nullifiers only and generalize the multimode entanglement from that. We plot optimal two-mode N_{10}^c (dark green dashed) in panel (c) for $\tilde{\Delta}\omega_{m_j}/g_1 \approx -0.6$, $\kappa_a/g_1 = 0.9$, $E_d = 2.4 \times 10^9$ MHz, and $g_j/2\pi = 1000$ MHz, along with other nullifiers, N_6^c (solid teal blue), N_7^c (dot-dashed brown), N_8^c (dotted light brown), and N_9^c (purple dashed), for the same parameters. The remaining parameters are the same as in Fig. 2. The inset shows $N_{1,\dots,5}^c$, where N_1^c shows the same behavior as N_{10}^c and must overlap, and the other three-mode nullifiers overlap altogether as well. Thus, simultaneously dropping below the shot noise of two-mode and three-mode nullifiers in linear and ring topologies is sufficient to generate multimode entanglement in $n = 10$ spheres and further for the generation of a cluster state.

Similarly, we plot the optimal three-mode nullifier N_9^c in panel (d) for $\tilde{\Delta}\omega_{m_j}/g_1 \approx -0.8$, $\kappa_a/g_1 = 1.65$, $E_d = 6.7 \times 10^{10}$ MHz, and for the same cavity-magnon couplings g_j as in panel (c), along with other nullifiers $N_{6,\dots,10}^c$ for the same parameters. The inset shows the remaining nullifiers $N_{1,\dots,5}^c$ for the same parameters. When all such nullifiers go below the shot noise, a cluster state is generated. This further generates entanglement in all the bipartitions $E_3^{(3)}$ of three modes, and all such combinations of ring topologies are enough to generate entanglement among ten spheres (see Sec. S4 of the Supplemental Material [78]). Thus, the ring topology of three entangled modes acts as a building block and can be scaled up to a large number of modes for the generation of entanglement (see Sec. S4 of the Supplemental Material [78]) and cluster states. We believe that a large number of modes can be entangled in this way, though they require advanced numerical techniques for optimization as the parameters shift with more drive power and Kerr interactions. It would be interesting to see the experimental demonstration of a 2D array of modes in an MW cavity where the ring topologies remain the same as presented here, though the conditional factor will be additional to optimize and generate the cluster states. However, the present proposal remains the minimal example with the weight factor (edges) equal to 1 and can be generalized to multiple spheres coupled to MW or optical cavity modes.

VI. DISCUSSION AND CONCLUSION

One-way quantum computing is a promising platform based on measurements on multiple entangled states—cluster states. Generating entanglement in optical systems relies on squeezed and two-mode squeezed interactions, though the optical interactions are weak. However, hybrid systems of magnons provide a framework of strong and ultrastrong couplings with nonlinear interactions such as self-Kerr or cross-Kerr that allow for the generation of entanglement when driven near and far from equilibrium [74]. Scaling such an entanglement over multiple YIG spheres ($n = 3, 5, 10$) allows us to generate graph states. Specifically, we show the results for the steady-state generation of cluster states of a few spheres with linear and ring topologies at $T = 100$ mK that can be generalized to multiple spheres. However, squeezing in each nullifier can be further improved by using additional cavity modes or exploiting full nonlinearity, where the former allows reducing the heating rate (through amplifications) and the latter, with full nonlinearity, will enhance single- and two-mode squeezing interactions by injecting more photons/magnons, thereby enhancing correlations and reducing noise together. In such systems, bistability [89] and multistability [72] often appear in the strong coupling. However, as we noted, the strong and ultrastrong couplings suppress the cooling of magnon modes as the cavity and magnon couple to each other strongly rather than to the bath. Our numerical optimization shows that optimal squeezing in nullifiers dominates in the dissipative cavity regimes. As long as the cavity-magnon coupling is smaller than the cavity linewidth, $\gamma_{m_j} < g_j < \kappa_a$, the avoided crossing (a signature of strong coupling) does not appear [40] and the system remains in a weak coupling regime. In addition, we expect monostability in our entire calculations (see Sec. S3 of the Supplemental Material [78]) for such a parameter regime.

In linear interactions, the dark mode (collective Bogoliubov mode) [90,91] often appears in a system of two oscillators coupled to a single-cavity mode, further suppressing the effective cooling and robust correlations. Cooling such a decoupled collective mode enhances the correlations and entanglement for thermal noise of occupations for 3 orders of magnitude [92] at mK temperature or 7 orders of magnitude [93] at room temperature. However, such modes in multiple YIG spheres are due to magnon-magnon interactions [66,94,95] with equal frequencies of the two modes and can be suppressed for unequal frequencies or by placing the spheres at a distance larger than the radius of each sphere [66]. Further, the nonlinear interactions in the present proposal allow many possibilities of hybrid modes (e.g., polaritons) instead of dark modes. However, the former remains complex to study with multiple modes. Moreover, optimizing over various parameters allows us to look into the parameter space, which is inaccessible through fixed parameters required for the dark modes. We show that for unequal detunings of magnon modes (see Fig. S6 in Sec. S5 of the Supplemental Material [78]), the quantumness further gets suppressed through thermalization instead of expecting more quantumness by breaking such modes, and thus, we rule out the possibility of such modes in our case. In addition, the versatility of nonlinearity can be seen for the parameter space while choosing equal and positive magnon detunings (see Fig. S5 in Sec. S5 of the Supplemental Material [78]) and positive Kerr nonlinearity (not shown), where cluster states can be generated, though it remains optimal for the parameters shown in Figs. 4 and 5.

We show that the present scheme of a few spheres, $n = 3$, with a gain in squeezing (≈2.2 dB), in a linear array can be generalized to multiple spheres inside an MW cavity to generate multimode entanglement and cluster states for different topologies. The present system with a large linewidth has measurement advantages as the tomography of magnon states requires an MW cavity to decay fast and measurement of entanglement through a weak probe field. Interestingly, the tomography of nullifiers requires measurement of a few elements of the covariance matrix rather than the full tomography of it, as required for the logarithmic negativity. For our numerical simulations, we choose experimentally feasible parameters with state-of-the-art techniques [40,41,45,96]. For example, we choose a range of drive power that satisfied the condition for magnon excitation $\langle m^\dagger m\rangle \ll 2n_s s = 5n_s$ [69,71,97] in a sphere of size $2r \approx 0.3$–0.5 mm [40,66], r being radius of a sphere, where drive power $P \approx 4$ mW for a linear and $P \approx 9$ mW for a ring topology of $n = 3$ spheres, $P \approx 8$ mW for a linear and $P \approx 0.1$ W for a ring topology of $n = 5$ and $P \approx 1$ mW for a linear and $P \approx 0.4$ W for a ring topology of $n = 10$ spheres. The power for linear topology of $n = 10$ remains $P \approx$ mW. However, for a slightly high diameter of spheres, which can be a few millimeters [40,66], a larger number of spins, the power for the ring topology of ten spheres will remain $P \leqslant 50$ mW. It is obvious that for a large number of modes, we require more power for the mean magnons than for a few modes. However, the system would be stable in a far-detuned cavity mode and further relaxed through a dissipative channel.

Very recently, a multimode cluster state has been demonstrated on an integrated optical chip [32] and with input of multiple frequencies [31] with 1.4 dB squeezing in a square-ladder nullifier. In addition, such self-Kerr nonlinearities allow the engineering of Fock states in the lossy systems [98,99] that have potential applications in quantum information processing. However, our scheme is more general and can be applied to diverse systems where similar nonlinearities are present, such as in optical fiber [100], microcavities [101], circuit QED [102], and atomic ensembles with intrinsic nonlinearities. Further, improving the squeezing of cluster states would allow applications in bosonic error correction through Gottesman-Kitaev-Preskill states [103–105] and multimode entanglement paves the way toward dark matter detection through hybrid systems [55,106]. The hybrid systems of magnons are versatile in terms of coupling strength, ranging from strong to ultrastrong, and coupling to different spin and bosonic systems, making them a potential platform for steering nonclassical Gaussian and non-Gaussian states in the near future for upcoming quantum technologies.

In conclusion, we present a scheme for generating macroscopic multimode entanglement and graph states of multiple YIG spheres in an MW cavity. The optimal such states require the cavity to be far-detuned and dissipative, which further allows the generalization of the scheme to multiple spheres. The dissipative cavity allows more cooling to the system, while the Kerr interactions with strong drive enhance mean numbers and collective squeezing of the modes, thereby generating multimode entanglement in the steady state of the system. We show the generation of Gaussian cluster states for a linear and a ring topology of $n = \{3, 5, 10\}$ YIG spheres within an MW cavity for realistic feasible parameters. Such multimode nonclassical states are central to the upcoming quantum technologies and pave the way toward quantum information and computing, metrology, advanced sensing, and quantum networks.

ACKNOWLEDGMENT

This work was supported by funding from the Okinawa Institute of Science and Technology Graduate University.

DATA AVAILABILITY

No data were created or analyzed in this study.

[1] C. Weedbrook, S. Pirandola, R. García-Patrón, N. J. Cerf, T. C. Ralph, J. H. Shapiro, and S. Lloyd, Gaussian quantum information, Rev. Mod. Phys. **84**, 621 (2012).

[2] S. L. Braunstein and P. van Loock, Quantum information with continuous variables, Rev. Mod. Phys. **77**, 513 (2005).

[3] C. Degen, F. Reinhard, and P. Cappellaro, Quantum sensing, Rev. Mod. Phys. **89**, 035002 (2017).

[4] S. Bose, I. Fuentes, A. A. Geraci, S. M. Khan, S. Qvarfort, M. Rademacher, M. Rashid, M. Toroš, H. Ulbricht, and C. C. Wanjura, Massive quantum systems as interfaces of quantum mechanics and gravity, Rev. Mod. Phys. **97**, 015003 (2025).

[5] R. Raussendorf and H. J. Briegel, A one-way quantum computer, Phys. Rev. Lett. **86**, 5188 (2001).

[6] N. C. Menicucci, P. van Loock, M. Gu, C. Weedbrook, T. C. Ralph, and M. A. Nielsen, Universal quantum computation with continuous-variable cluster states, Phys. Rev. Lett. **97**, 110501 (2006).

[7] N. C. Menicucci, Fault-tolerant measurement-based quantum computing with continuous-variable cluster states, Phys. Rev. Lett. **112**, 120504 (2014).

[8] M. Walschaers, Non-Gaussian quantum states and where to find them, PRX Quantum **2**, 030204 (2021).

[9] Y. S. Ra, A. Dufour, M. Walschaers, C. Jacquard, T. Michel, C. Fabre, and N. Treps, Non-Gaussian quantum states of a multimode light field, Nat. Phys. **16**, 144 (2019).

[10] S. Wehner, D. Elkouss, and R. Hanson, Quantum internet: A vision for the road ahead, Science **362**, eaam9288 (2018).

[11] H. J. Briegel, D. E. Browne, W. Dür, R. Raussendorf, and M. Van den Nest, Measurement-based quantum computation, Nat. Phys. **5**, 19 (2009).

[12] P. van Loock and S. L. Braunstein, Multipartite entanglement for continuous variables: A quantum teleportation network, Phys. Rev. Lett. **84**, 3482 (2000).

[13] M. Hein, J. Eisert, and H. J. Briegel, Multiparty entanglement in graph states, Phys. Rev. A **69**, 062311 (2004).

[14] J. Zhang and S. L. Braunstein, Continuous-variable Gaussian analog of cluster states, Phys. Rev. A **73**, 032318 (2006).

[15] P. van Loock, C. Weedbrook, and M. Gu, Building Gaussian cluster states by linear optics, Phys. Rev. A **76**, 032321 (2007).

[16] P. van Loock, Examples of Gaussian cluster computation, J. Opt. Soc. Am. B **24**, 340 (2007).

[17] M. Yukawa, R. Ukai, P. van Loock, and A. Furusawa, Experimental generation of four-mode continuous-variable cluster states, Phys. Rev. A **78**, 012301 (2008).

[18] Y. Miwa, R. Ukai, J.-I. Yoshikawa, R. Filip, P. van Loock, and A. Furusawa, Demonstration of cluster-state shaping and quantum erasure for continuous variables, Phys. Rev. A **82**, 032305 (2010).

[19] N. C. Menicucci, S. T. Flammia, and P. van Loock, Graphical calculus for Gaussian pure states, Phys. Rev. A **83**, 042335 (2011).

[20] M. Gu, C. Weedbrook, N. C. Menicucci, T. C. Ralph, and P. van Loock, Quantum computing with continuous-variable clusters, Phys. Rev. A **79**, 062318 (2009).

[21] C. González-Arciniegas, P. Nussenzveig, M. Martinelli, and O. Pfister, Cluster states from Gaussian states: Essential diagnostic tools for continuous-variable one-way quantum computing, PRX Quantum **2**, 030343 (2021).

[22] V. S. Ferreira, G. Kim, A. Butler, H. Pichler, and O. Painter, Deterministic generation of multidimensional photonic cluster states with a single quantum emitter, Nat. Phys. **20**, 865 (2024).

[23] S. Armstrong, J.-F. Morizur, J. Janousek, B. Hage, N. Treps, P. K. Lam, and H.-A. Bachor, Programmable multimode quantum networks, Nat. Commun. **3**, 1026 (2012).

[24] R. Pooser and J. Jing, Continuous-variable cluster-state generation over the optical spatial mode comb, Phys. Rev. A **90**, 043841 (2014).

[25] S. Yokoyama, R. Ukai, S. C. Armstrong, C. Sornphiphatphong, T. Kaji, S. Suzuki, J.-I. Yoshikawa, H. Yonezawa, N. C. Menicucci, and A. Furusawa, Ultra-large-scale continuous-variable cluster states multiplexed in the time domain, Nat. Photon. **7**, 982 (2013).

[26] J.-I. Yoshikawa, S. Yokoyama, T. Kaji, C. Sornphiphatphong, Y. Shiozawa, K. Makino, and A. Furusawa, Invited article: Generation of one-million-mode continuous-variable cluster state by unlimited time-domain multiplexing, APL Photon. **1**, 060801 (2016).

[27] M. V. Larsen, X. Guo, C. R. Breum, J. S. Neergaard-Nielsen, and U. L. Andersen, Deterministic generation of a two-dimensional cluster state, Science **366**, 369 (2019).

[28] W. Asavanant, Y. Shiozawa, S. Yokoyama, B. Charoensombutamon, H. Emura, R. N. Alexander, S. Takeda, J. I. Yoshikawa, N. C. Menicucci, H. Yonezawa, and A. Furusawa, Generation of time-domain-multiplexed two-dimensional cluster state, Science **366**, 373 (2019).

[29] M. Chen, N. C. Menicucci, and O. Pfister, Experimental realization of multipartite entanglement of 60 modes of a quantum optical frequency comb, Phys. Rev. Lett. **112**, 120505 (2014).

[30] Y. Cai, J. Roslund, G. Ferrini, F. Arzani, X. Xu, C. Fabre, and N. Treps, Multimode entanglement in reconfigurable graph states using optical frequency combs, Nat. Commun. **8**, 15645 (2017).

[31] F. Lingua, J. Rivera Hernández, M. Cortinovis, and D. B. Haviland, Continuous-variable square-ladder cluster states in a microwave frequency comb, Phys. Rev. Lett. **134**, 183602 (2025).

[32] X. Jia, C. Zhai, X. Zhu, C. You, Y. Cao, X. Zhang, Y. Zheng, Z. Fu, J. Mao, T. Dai, L. Chang, X. Su, Q. Gong, and J. Wang, Continuous-variable multipartite entanglement in an integrated microcomb, Nature (London) **639**, 329 (2025).

[33] P. C. Humphreys, W. S. Kolthammer, J. Nunn, M. Barbieri, A. Datta, and I. A. Walmsley, Continuous-variable quantum computing in optical time-frequency modes using quantum memories, Phys. Rev. Lett. **113**, 130502 (2014).

[34] B.-H. Wu, R. N. Alexander, S. Liu, and Z. Zhang, Quantum computing with multidimensional continuous-variable cluster states in a scalable photonic platform, Phys. Rev. Res. **2**, 023138 (2020).

[35] R. Yang, J. Zhang, I. Klich, C. González-Arciniegas, and O. Pfister, Spatiotemporal graph states from a single optical parametric oscillator, Phys. Rev. A **101**, 043832 (2020).

[36] O. Houhou, H. Aissaoui, and A. Ferraro, Generation of cluster states in optomechanical quantum systems, Phys. Rev. A **92**, 063843 (2015).

[37] N. Yazdi, S. Zippilli, and D. Vitali, Generation of stable Gaussian cluster states in optomechanical systems with multifrequency drives, Quantum Sci. Technol. **9**, 035001 (2024).

[38] X. Yao, M. H. de Jong, J. Li, and S. Gröblacher, Long-range optomechanical interactions in SiN membrane arrays, Phys. Rev. X **15**, 011014 (2025).

[39] G. Kurizki, P. Bertet, Y. Kubo, K. Mølmer, D. Petrosyan, P. Rabl, and J. Schmiedmayer, Quantum technologies with hybrid systems, Proc. Natl. Acad. Sci. USA **112**, 3866 (2015).

[40] X. Zhang, C.-L. Zou, L. Jiang, and H. X. Tang, Strongly coupled magnons and cavity microwave photons, Phys. Rev. Lett. **113**, 156401 (2014).

[41] Y. Tabuchi, S. Ishino, T. Ishikawa, R. Yamazaki, K. Usami, and Y. Nakamura, Hybridizing ferromagnetic magnons and microwave photons in the quantum limit, Phys. Rev. Lett. **113**, 083603 (2014).

[42] D. Lachance-Quirion, Y. Tabuchi, A. Gloppe, K. Usami, and Y. Nakamura, Hybrid quantum systems based on magnonics, Appl. Phys. Express **12**, 070101 (2019).

[43] B. Zare Rameshti, S. Viola Kusminskiy, J. A. Haigh, K. Usami, D. Lachance-Quirion, Y. Nakamura, C.-M. Hu, H. X. Tang, G. E. Bauer, and Y. M. Blanter, Cavity magnonics, Phys. Rep. **979**, 1 (2022).

[44] Y. Tabuchi, S. Ishino, A. Noguchi, T. Ishikawa, R. Yamazaki, K. Usami, and Y. Nakamura, Coherent coupling between a ferromagnetic magnon and a superconducting qubit, Science **349**, 405 (2015).

[45] X. Zhang, C.-L. Zou, L. Jiang, and H. X. Tang, Cavity magnomechanics, Sci. Adv. **2**, e1501286 (2016).

[46] W. Xiong, M. Tian, G.-Q. Zhang, and J. Q. You, Strong long-range spin-spin coupling via a Kerr magnon interface, Phys. Rev. B **105**, 245310 (2022).

[47] A. B. Solanki, S. I. Bogdanov, M. M. Rahman, A. Rustagi, N. R. Dilley, T. Shen, W. Tong, P. Debashis, Z. Chen, J. Appenzeller, Y. P. Chen, V. M. Shalaev, and P. Upadhyaya, Electric field control of interaction between magnons and quantum spin defects, Phys. Rev. Res. **4**, L012025 (2022).

[48] Y. Li, W. Zhang, V. Tyberkevych, W.-K. Kwok, A. Hoffmann, and V. Novosad, Hybrid magnonics: Physics, circuits, and applications for coherent information processing, J. Appl. Phys. **128**, 130902 (2020).

[49] H. Yuan, Y. Cao, A. Kamra, R. A. Duine, and P. Yan, Quantum magnonics: When magnon spintronics meets quantum information science, Phys. Rep. **965**, 1 (2022).

[50] E. Callen, Magnetostriction, J. Appl. Phys. **39**, 519 (1968).

[51] H. Keshtgar, M. Zareyan, and G. E. Bauer, Acoustic parametric pumping of spin waves, Solid State Commun. **198**, 30 (2014).

[52] C. Gonzalez-Ballestero, J. Gieseler, and O. Romero-Isart, Quantum acoustomechanics with a micromagnet, Phys. Rev. Lett. **124**, 093602 (2020).

[53] C. A. Potts, E. Varga, V. A. Bittencourt, S. V. Kusminskiy, and J. P. Davis, Dynamical backaction magnomechanics, Phys. Rev. X **11**, 031053 (2021).

[54] D. Lachance-Quirion, Y. Tabuchi, S. Ishino, A. Noguchi, T. Ishikawa, R. Yamazaki, and Y. Nakamura, Resolving quanta of collective spin excitations in a millimeter-sized ferromagnet, Sci. Adv. **3**, e1603150 (2017).

[55] D. Lachance-Quirion, S. P. Wolski, Y. Tabuchi, S. Kono, K. Usami, and Y. Nakamura, Entanglement-based single-shot detection of a single magnon with a superconducting qubit, Science **367**, 425 (2020).

[56] A. Kani, B. Sarma, and J. Twamley, Intensive cavity-magnomechanical cooling of a levitated macromagnet, Phys. Rev. Lett. **128**, 013602 (2022).

[57] A. Kumar Chauhan, A. Kani, and J. Twamley, Enhancing macroscopic multimode entanglement through many-body interactions in cavity magnomechanics, Phys. Rev. A **111**, 033505 (2025).

[58] M. Elyasi, Y. M. Blanter, and G. E. W. Bauer, Resources of nonlinear cavity magnonics for quantum information, Phys. Rev. B **101**, 054402 (2020).

[59] V. A. S. V. Bittencourt, C. A. Potts, Y. Huang, J. P. Davis, and S. V. Kusminskiy, Magnomechanical backaction corrections due to coupling to higher-order walker modes and Kerr nonlinearities, Phys. Rev. B **107**, 144411 (2023).

[60] J. Li, S.-Y. Zhu, and G. S. Agarwal, Squeezed states of magnons and phonons in cavity magnomechanics, Phys. Rev. A **99**, 021801 (2019).

[61] Z.-Y. Fan, H.-B. Zhu, H.-T. Li, and J. Li, Magnon squeezing via reservoir-engineered optomagnomechanics, APL Photon. **9**, 100804 (2024).

[62] J. Li, S.-Y. Zhu, and G. Agarwal, Magnon-photon-phonon entanglement in cavity magnomechanics, Phys. Rev. Lett. **121**, 203601 (2018).

[63] A. Kamra, W. Belzig, and A. Brataas, Magnon-squeezing as a niche of quantum magnonics, Appl. Phys. Lett. **117**, 090501 (2020).

[64] J. Zou, S. K. Kim, and Y. Tserkovnyak, Tuning entanglement by squeezing magnons in anisotropic magnets, Phys. Rev. B **101**, 014416 (2020).

[65] J. M. Lee, H.-W. Lee, and M.-J. Hwang, Cavity magnonics with easy-axis ferromagnets: Critically enhanced magnon squeezing and light-matter interaction, Phys. Rev. B **108**, L241404 (2023).

[66] N. Crescini, C. Braggio, G. Carugno, A. Ortolan, and G. Ruoso, Coherent coupling between multiple ferrimagnetic spheres and a microwave cavity at millikelvin temperatures, Phys. Rev. B **104**, 064426 (2021).

[67] S. Blundell, *Magnetism in Condensed Matter* (Oxford University Press, Oxford, 2001).

[68] J. C. Slonczewski, Anisotropy and magnetostriction in magnetic oxides, J. Appl. Phys. **32**, S253 (1961).

[69] Y.-P. Wang, G.-Q. Zhang, D. Zhang, X.-Q. Luo, W. Xiong, S.-P. Wang, T.-F. Li, C.-M. Hu, and J. Q. You, Magnon Kerr effect in a strongly coupled cavity-magnon system, Phys. Rev. B **94**, 224410 (2016).

[70] S. Zheng, Z. Wang, Y. Wang, F. Sun, Q. He, P. Yan, and H. Y. Yuan, Tutorial: Nonlinear magnonics, J. Appl. Phys. **134**, 151101 (2023).

[71] Y.-P. Wang, G.-Q. Zhang, D. Zhang, T.-F. Li, C.-M. Hu, and J. You, Bistability of cavity magnon polaritons, Phys. Rev. Lett. **120**, 057202 (2018).

[72] R.-C. Shen, Y.-P. Wang, J. Li, S.-Y. Zhu, G. Agarwal, and J. You, Long-time memory and ternary logic gate using a multistable cavity magnonic system, Phys. Rev. Lett. **127**, 183202 (2021).

[73] J. M. P. Nair, Z. Zhang, M. O. Scully, and G. S. Agarwal, Nonlinear spin currents, Phys. Rev. B **102**, 104415 (2020).

[74] Z. Zhang, M. O. Scully, and G. S. Agarwal, Quantum entanglement between two magnon modes via Kerr nonlinearity driven far from equilibrium, Phys. Rev. Res. **1**, 023021 (2019).

[75] D. Zhang, X. Q. Luo, Y. P. Wang, T. F. Li, and J. Q. You, Observation of the exceptional point in cavity magnon-polaritons, Nat. Commun. **8**, 1 (2017).

[76] A. Frisk Kockum, A. Miranowicz, S. De Liberato, S. Savasta, and F. Nori, Ultrastrong coupling between light and matter, Nat. Rev. Phys. **1**, 19 (2019).

[77] G. Bourcin, J. Bourhill, V. Vlaminck, and V. Castel, Strong to ultrastrong coherent coupling measurements in a YIG/cavity system at room temperature, Phys. Rev. B **107**, 214423 (2023).

[78] See Supplemental Material at http://link.aps.org/supplemental/10.1103/6cpk-xcw4 for detailed information on Kerr nonlinearity and cluster states, which includes Refs. [107,108]. Additional plots for mean numbers versus drive power, multimode entanglement for $n = 10$ spheres, and cluster states for positive and unequal magnon detunings are shown.

[79] A. Bacciotti, Stability and control of linear systems, studies in systems, *Decision and Control* (Springer Nature Switzerland, 2019), Vol. 185.

[80] O. Pfister, Continuous-variable quantum computing in the quantum optical frequency comb, J. Phys. B: At. Mol. Opt. Phys. **53**, 012001 (2020).

[81] P. van Loock and A. Furusawa, Detecting genuine multipartite continuous-variable entanglement, Phys. Rev. A **67**, 052315 (2003).

[82] G. Vidal and R. F. Werner, Computable measure of entanglement, Phys. Rev. A **65**, 032314 (2002).

[83] R. Simon, Peres-Horodecki separability criterion for continuous variable systems, Phys. Rev. Lett. **84**, 2726 (2000).

[84] L.-M. Duan, G. Giedke, J. I. Cirac, and P. Zoller, Inseparability criterion for continuous variable systems, Phys. Rev. Lett. **84**, 2722 (2000).

[85] A. K. Chauhan, O. Černotík, and R. Filip, Tuneable Gaussian entanglement in levitated nanoparticle arrays, npj Quantum Inf. **8**, 151 (2022).

[86] M. Hein, W. Dür, J. Eisert, R. Raussendorf, M. Nest, and H.-J. Briegel, Entanglement in graph states and its applications, arXiv:quant-ph/0602096.

[87] C. Meignant, D. Markham, and F. Grosshans, Distributing graph states over arbitrary quantum networks, Phys. Rev. A **100**, 052333 (2019).

[88] R. F. Werner and M. M. Wolf, Bound entangled Gaussian states, Phys. Rev. Lett. **86**, 3658 (2001).

[89] Z.-B. Yang, H. Jin, J.-W. Jin, J.-Y. Liu, H.-Y. Liu, and R.-C. Yang, Bistability of squeezing and entanglement in cavity magnonics, Phys. Rev. Res. **3**, 023126 (2021).

[90] L. Tian, Adiabatic state conversion and pulse transmission in optomechanical systems, Phys. Rev. Lett. **108**, 153604 (2012).

[91] Y.-D. Wang and A. A. Clerk, Using interference for high fidelity quantum state transfer in optomechanics, Phys. Rev. Lett. **108**, 153603 (2012).

[92] D.-G. Lai, J.-Q. Liao, A. Miranowicz, and F. Nori, Noise-tolerant optomechanical entanglement via synthetic magnetism, Phys. Rev. Lett. **129**, 063602 (2022).

[93] A. K. Chauhan, O. Černotík, and R. Filip, Stationary Gaussian entanglement between levitated nanoparticles, New J. Phys. **22**, 123021 (2020).

[94] X. Zhang, C.-L. Zou, N. Zhu, F. Marquardt, L. Jiang, and H. X. Tang, Magnon dark modes and gradient memory, Nat. Commun. **6**, 8914 (2015).

[95] M. X. Bi, X. H. Yan, Y. Xiao, and C. J. Dai, Magnon dark mode in a strong driving microwave cavity, J. Appl. Phys. **126**, 173902 (2019).

[96] J. T. Hou and L. Liu, Strong coupling between microwave photons and nanomagnet magnons, Phys. Rev. Lett. **123**, 107702 (2019).

[97] D. Zhang, X.-M. Wang, T.-F. Li, X.-Q. Luo, W. Wu, F. Nori, and J. You, Cavity quantum electrodynamics with ferromagnetic magnons in a small yttrium-iron-garnet sphere, npj Quantum Inf. **1**, 15014 (2015).

[98] A. Lingenfelter, D. Roberts, and A. A. Clerk, Unconditional fock state generation using arbitrarily weak photonic nonlinearities, Sci. Adv. **7**, eabj1916 (2021).

[99] M. Yuan, A. Seif, A. Lingenfelter, D. I. Schuster, A. A. Clerk, and L. Jiang, Universal control in bosonic systems with weak Kerr nonlinearities, Phys. Rev. A **111**, 032606 (2025).

[100] N. Matsuda, R. Shimizu, Y. Mitsumori, H. Kosaka, and K. Edamatsu, Observation of optical-fibre Kerr nonlinearity at the single-photon level, Nat. Photon. **3**, 95 (2009).

[101] H. Rokhsari and K. J. Vahala, Observation of Kerr nonlinearity in microcavities at room temperature, Opt. Lett. **30**, 427 (2005).

[102] S. Rebić, J. Twamley, and G. J. Milburn, Giant Kerr nonlinearities in circuit quantum electrodynamics, Phys. Rev. Lett. **103**, 150503 (2009).

[103] B. W. Walshe, B. Q. Baragiola, R. N. Alexander, and N. C. Menicucci, Continuous-variable gate teleportation and bosonic-code error correction, Phys. Rev. A **102**, 062411 (2020).

[104] B. W. Walshe, R. N. Alexander, N. C. Menicucci, and B. Q. Baragiola, Streamlined quantum computing with macronode cluster states, Phys. Rev. A **104**, 062427 (2021).

[105] P. Du, J. Zhang, T. Zhang, R. Yang, and J. Gao, A complete continuous-variable quantum computation architecture based on the 2D spatiotemporal cluster state, Sci. Rep. **15**, 1 (2025).

[106] G. Flower, J. Bourhill, M. Goryachev, and M. E. Tobar, Broadening frequency range of a ferromagnetic axion haloscope with strongly coupled cavity–magnon polaritons, Phys. Dark Universe **25**, 100306 (2019).

[107] J. C. Slonczewski, Origin of magnetic anisotropy in cobalt-substituted magnetite, Phys. Rev. **110**, 1341 (1958).

[108] T. Holstein and H. Primakoff, Field dependence of the intrinsic domain magnetization of a ferromagnet, Phys. Rev. **58**, 1098 (1940).